



Nonequilibrium statistical thermodynamics of multicomponent interfaces

Phillip M. Rauscher^a, Hans Christian Öttinger^{b,1}, and Juan J. de Pablo^{a,c,d,1}

Edited by Christopher Jarzynski, University of Maryland, College Park, MD; received November 25, 2021; accepted March 24, 2022

Nonequilibrium interfacial thermodynamics has important implications for crucial biological, physical, and industrial-scale transport processes. Here, we discuss a theory of local equilibrium for multiphase multicomponent interfaces that builds upon the “sharp” interface concept first introduced by Gibbs, allowing for a description of nonequilibrium interfacial processes such as those arising in evaporation, condensation, adsorption, etc. By requiring that the thermodynamics be insensitive to the precise location of the dividing surface, one can identify conditions for local equilibrium and develop methods for measuring the values of intensive variables at the interface. We then use extensive, high-precision nonequilibrium molecular dynamics (NEMD) simulations to verify the theory and establish the validity of the local equilibrium hypothesis. In particular, we demonstrate that equilibrium equations of state are also valid out of equilibrium, and can be used to determine interfacial temperature and chemical potential(s) that are consistent with nonequilibrium generalizations of the Clapeyron and Gibbs adsorption equations. We also show, for example, that, far from equilibrium, temperature or chemical potential differences need not be uniform across an interface and may instead exhibit pronounced discontinuities. However, even in these circumstances, we demonstrate that the local equilibrium hypothesis and its implications remain valid. These results provide a thermodynamic foundation and computational tools for studying or revisiting a wide variety of interfacial transport phenomena.

interfaces | transport | nonequilibrium thermodynamics | molecular dynamics | statistical mechanics

Interfaces and interfacial effects are critically important in many areas of physics, chemistry, biology, medicine, and engineering (1–3). In many such cases, interfaces exist in nonequilibrium systems and play an active role in transport processes, thereby motivating multiple efforts to develop a thermodynamically consistent description of nonequilibrium interfaces (2–4) capable of describing complex interfacial processes (5, 6). These thermodynamics, however, are quite subtle and must be developed with care, as many of the standard equations and methods of bulk transport are not always applicable to interfacial systems (3). Here, we discuss a recently developed nonequilibrium thermodynamic theory of interfacial transport and use molecular dynamics (MD) simulations to validate the approach for multicomponent heterogeneous systems. Our findings serve to establish a thermodynamically consistent framework for analyzing and modeling complex interfacial transport processes.

To understand the challenges in describing interfacial transport, it is helpful to first recall the foundations of bulk transport phenomena (4, 7), whose governing equations rest on two fundamental pillars. First, balance equations for conserved quantities (e.g., mass, species mass, energy, and momentum) describe the time evolution of these quantities in terms of associated fluxes. These equations are formally exact, but can only be solved by introducing constitutive equations that relate the underlying fluxes to their spatial gradients, that is, thermodynamic forces. To obtain these relations, a second key ingredient of transport phenomena is introduced: the assumption of local thermodynamic equilibrium. One assumes that the overall system, which is not in equilibrium, may be divided into small (but still macroscopic) volumes that are. Thus, spatially varying values of the intensive thermodynamic quantities can be assigned, and the equilibrium thermodynamic relations (Euler, Gibbs–Duhem, etc.) and equations of state (8) are locally valid. The combination of balance equations and local equilibrium leads to an expression for local entropy production, which is assumed to be nonnegative (again, by virtue of equilibrium thermodynamics). One can then postulate thermodynamically informed constitutive relations and obtain the well-known equations of transport phenomena (Navier–Stokes–Fourier, Maxwell–Stefan, etc.). We stress that, while the balance equations are formally exact and rely only on well-established conservation principles, the assumption of local equilibrium is just that: an assumption. In bulk systems, this assumption is usually well

Significance

Interfaces and their dynamics are critical in many biological, physical, and industrial processes. However, the thermodynamics of interfaces far from equilibrium are subtle and have not been firmly or rigorously established. In analogy with well-known bulk phenomena, we hypothesize a “local” equilibrium for interfaces in multicomponent, multiphase systems and examine the resulting theoretical implications. We then conduct high-precision molecular dynamics simulations to validate the underlying theory, and show that generalized equilibrium thermodynamic equations can be applied to systems far beyond equilibrium. These results lay the groundwork for accurate and thermodynamically consistent modeling of transport at interfaces.

Author contributions: P.M.R., H.C.Ö., and J.J.d.P. designed research; P.M.R. performed research; P.M.R. and H.C.Ö. analyzed data; and P.M.R., H.C.Ö., and J.J.d.P. wrote the paper.

The authors declare no competing interest.

This article is a PNAS Direct Submission.

Copyright © 2022 the Author(s). Published by PNAS. This article is distributed under [Creative Commons Attribution-NonCommercial-NoDerivatives License 4.0 \(CC BY-NC-ND\)](https://creativecommons.org/licenses/by-nc-nd/4.0/).

¹To whom correspondence may be addressed. Email: hco@mat.ethz.ch or depablo@uchicago.edu.

This article contains supporting information online at <https://www.pnas.org/lookup/suppl/doi:10.1073/pnas.2121405119/-DCSupplemental>.

Published June 8, 2022.

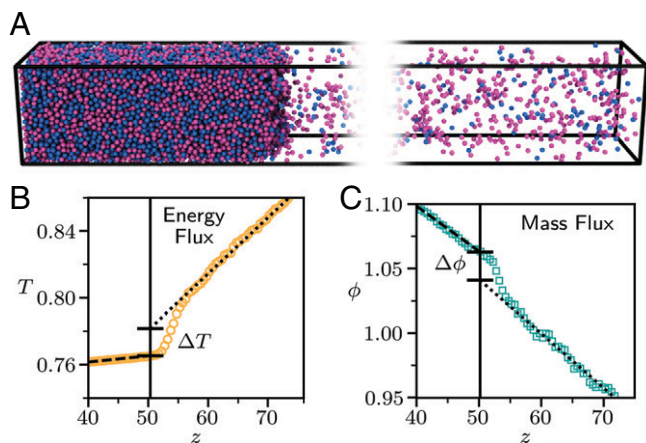


Fig. 1. (A) Visualization of the binary liquid/vapor system studied by MD simulations. The middle portion of the vapor phase has been omitted for clarity. (B) Demonstration of a temperature jump at the interface in a system subject to driven energy flux. The vertical line is the approximate position of the interface. (C) Demonstration of an interfacial jump in the chemical potential difference, $\phi \equiv \mu_1 - \mu_2$, in a system with driven species mass flux. The vertical line again represents the approximate position of the interface.

justified because the mean free path and collision frequencies of molecules in condensed phases are typically much smaller and faster, respectively, than the macroscopic length/time scales of interest, thereby allowing intermolecular collisions to induce local thermalization (7). Indeed, even for very strong flows, the differences in intensive variables across the length scales required for thermalization are usually small or negligible. Of course, many systems exist which do not satisfy this requirement [for instance, rarefied gas flows (9, 10)], but here we restrict ourselves to the more common situations for which local equilibrium is valid in the bulk.

In describing interfacial transport phenomena, we require analogous balance equations and local equilibrium assumptions. The former can readily be extended to interfaces rigorously, albeit with more complicated mathematics (2, 3). Likewise, we assume that interfaces will relax to quasi-equilibrium states very rapidly, as they are in intimate contact with the bulk phases. As a result, we postulate that these states may be characterized by equilibrium thermodynamic quantities that obey equilibrium interfacial equations of state. However, the situation is actually far more delicate than in the bulk, as the length scale of the interface is comparable to molecular dimensions, making the assumption of local thermalization highly suspect in such circumstances.

The associated challenges may be more easily appreciated by considering a simple test system. Fig. 1A shows a nonequilibrium MD (NEMD) simulation of a binary mixture of Lennard-Jones particles with coexisting liquid and vapor phases (see *Materials and Methods* for details). When subjected to heat/energy or species mass fluxes, the system develops temperature and chemical potential gradients, shown in Fig. 1B and C, respectively. It is immediately apparent that both intensive and extensive thermodynamic quantities vary rapidly through the interface. In fact, the bulk temperature and chemical potential profiles imply macroscopic

discontinuities (also called “jumps”) in intensive variables at the interface. Such jumps are also observed experimentally and can be quite significant. For example, the evaporation of water is associated with interfacial temperature jumps of up to 15 K (12, 13), while the condensation of mercury exhibits temperature jumps of over 70 K (14). Similar discontinuities in chemical potentials are less accessible experimentally, but arise quite clearly in simulations (Fig. 1C). In light of these complications, one must grapple with several key questions:

- 1) Clearly, the validity of the local equilibrium assumption cannot be taken for granted at interfaces, and must, instead, be established empirically. By what means can this be accomplished?
- 2) In order to use a local interfacial equilibrium in a macroscopic description of transport, we must be able to ascribe intensive quantities to the interface. How can one do so when the microscopic profiles in Fig. 1B and C are not accessible experimentally, and the bulk temperature profiles imply discontinuities?
- 3) Even if one could obtain microscopic temperature or chemical potential profiles (for instance, via molecular simulation), what is the “correct” position of the interface? Even microscopically small changes in the interface position can lead to large changes in the apparent intensive quantities with macroscopic implications.

With the goal of addressing these issues, in what follows, we first discuss the thermodynamic description of interfaces, and describe a framework within which we may test the local equilibrium hypothesis. We then conduct detailed, high-precision MD simulations to verify the hypothesis for a binary liquid–vapor system subject to both energy and mass flux (Fig. 1A). We further show how equilibrium equations of state can be used to determine the intensive quantities of the interface in nonequilibrium conditions—a procedure that does not depend on the precise position of the interface. These results lay a foundation for thermodynamically consistent modeling of interfacial processes in systems far from equilibrium.

Background

The study of interfaces plays a major role in the history of molecular science and engineering. The many surprising effects of capillarity, for example, were among the phenomena that suggested the molecular picture of matter in the 19th century (1). While a number of different thermodynamic descriptions of interfaces have been put forward, most may be grouped into one of two principal categories: 1) the “sharp” interface of Gibbs (15) and 2) the “diffuse” interface of van der Waals (16) and, later, Cahn and Hilliard (17) and Cahn (18). Both frameworks are commonly used to model interfacial transport (6), and local equilibrium must therefore be assessed in both pictures. We first discuss the diffuse interface model, and identify its shortcomings in the context of the analysis of local equilibrium. We then introduce the sharp interface framework, and outline the nonequilibrium theory in the following section.

Diffuse Interfaces. The diffuse interface viewpoint rests on the fact that microscopic densities vary rapidly but continuously through the interface. To capture the thermodynamic cost of such density inhomogeneities, the local free energy of the system is augmented to include square gradient terms of the form $|\nabla\psi|^2$, where ψ is some scalar field (e.g., mass density, volume/mole fraction, or other auxiliary field). The approach is closely related to

*Although heat and energy fluxes are intimately related, it is more common, in the experimental literature, to work with the former, as these may be directly measured. However, in thermodynamic theories such as the one discussed here, the quantity that arises more naturally is, in fact, the energy flux (4, 7, 11). Moreover, in molecular simulations, the measurement of heat fluxes in multicomponent systems requires cumbersome calculations of partial molar enthalpies. We prefer to avoid these complications and so discuss our results in terms of the energy flux. Nevertheless, for the purposes of this work, the reader may, in fact, consider the two as conceptually interchangeable without issue.

density functional theory, and the gradient terms can be derived in this framework via a Taylor expansion of the free energy functional with respect to the order parameters ψ (6). The interface is thus described in the same manner as the bulk phases, rather than as an autonomous two-dimensional object. To obtain the equilibrium interfacial density profile, one typically minimizes the free energy through a variational approach and solves the resulting equations (usually numerically); these methods have been used to study a wide variety of equilibrium systems. Such treatments are also known as “phase field” models in the literature. To obtain nonequilibrium evolution equations for phase field models, one combines the free energy functional with bulk balance equations and (typically linear) constitutive relations. The resulting equations are identical to those of bulk fluids, but with a modified pressure expression that includes the contribution of the gradient terms.

The diffuse interface model is powerful and widely used, especially when the length scale of interest is comparable to that of the interface itself. It can also be attractive from a numerical perspective. In such cases, it is often considerably more convenient than the sharp interface description, for instance, in describing near-critical fluids, contact lines, mixing processes, or nucleation (6, 19). However, it does have some drawbacks as a thermodynamic theory. For example, phase field models rely on free energy functionals that are essentially coarse-grained descriptions of the system. It is therefore unclear whether the same functional(s) is(are) valid out of equilibrium, especially at the interface, where the relationships between thermodynamic variables need not be the same as in the bulk (1). Thus, most treatments inherently assume that local equilibrium is valid through the entire interfacial region, but, as discussed earlier, the local equilibrium of interfaces is not obvious and must be demonstrated and tested.

Local equilibrium in the context of the diffuse interface framework is a subtle issue, whose difficulty may be traced back to the fundamental underlying assumptions of the theory. The classic derivation of Cahn and Hilliard (17) and Cahn (18) requires that $|\nabla\psi| \ll b^{-1}$, where b is the range of the direct correlation function (i.e., the interparticle potential). While this condition is easily satisfied in bulk phases (even out of equilibrium), the two quantities are of the same order of magnitude at the interface for many systems (*SI Appendix*). As a result, the profiles of certain thermodynamic variables through the interface are microscopically ill defined (1). For instance, one would obtain a different energy profile by assigning each pair of interacting particles one-half of the interaction energy versus “smearing” the interaction energy uniformly along the line between the particles [as done by Kirkwood and Buff (20) and Irving and Kirkwood (21)]. All such choices are inherently arbitrary and lead to different results; thus, local fields are not well defined at the interface for internal energy, entropy, and stress, among others, and, consequently, the fluxes of these quantities are also not well defined. There are, of course, certain constraints that these profiles must satisfy, but these are given in terms of their integrals, which, as described later on, make reference to a sharp interface. The lack of well-defined local profiles for energy and entropy is a challenge for two reasons: 1) these quantities are the generators of reversible and irreversible nonequilibrium dynamics, respectively (22–24), making nonequilibrium modeling difficult, and 2) it is unclear how the local equilibrium hypothesis may be understood and tested within this framework. In fact, the issues described above apply also to heterogeneous systems in global equilibrium.

As hinted above, although the interfacial profiles of thermodynamic quantities in the diffuse model are not well defined, their integrals are; any ambiguity in the locus of the interaction

energy/stress/etc. is circumvented when integrating over distances that are large compared to the particle interaction range by virtue of conservation laws. These integrals are closely related to so-called surface excess quantities that form the basis of the sharp interface description advanced by Gibbs (1, 15). For these reasons, the sharp interface model is better suited for studying local equilibrium compared to the diffuse model, as discussed in the next section.

Sharp Interfaces. In the classic picture proposed by Gibbs (15), a two-phase system comprises the bulk phases and a sharp, two-dimensional dividing surface. Associated with this surface are excess densities of extensive quantities (also called surface functions), which arise because the relevant thermodynamic variables vary rapidly but continuously through the interfacial region. Meanwhile, at equilibrium, the temperature and chemical potential(s) of the interface are the same as those of the adjacent bulk phases. Other intensive quantities, such as surface tension and bending stiffness, arise from mechanical properties of the interface and are the subject of interfacial rheology. Indeed, most rheological constitutive equations for interfaces are formulated within the sharp interface framework. Note also that such sharp interfaces are routinely used as boundary conditions in the study of transport problems. These considerations make the sharp dividing surface model an appealing foundation for a nonequilibrium thermodynamics of interfaces.

Consider a planar interface with the z axis normal to the surface. The values of the excess densities mentioned above depend on the precise location of the interface, z^s , which is chosen a priori arbitrarily. Since the extensive density profiles vary rapidly through the narrow interfacial region, even small changes in the position of the interface (e.g., on the order of the molecular size) can lead to large changes in the excess quantities, which may even change sign. Concretely, the excess density $a^s(z^s)$ of some extensive quantity, a , is given in terms of the extrapolated bulk density profiles in the two phases, $a^I(z)$ and $a^{II}(z)$ (both constant at equilibrium), and an “apparent” microscopic profile, $a(z)$, as follows:

$$a^s(z^s) = \int_{-\infty}^{z^s} [a(z) - a^I(z)] dz + \int_{z^s}^{\infty} [a(z) - a^{II}(z)] dz, \quad [1]$$

where phase I corresponds to the region of smaller z , and the integration limits are assumed to be far enough from the interfacial region that the profiles $a(z)$ and $a^{I/II}$ become equivalent. We again stress that, for many quantities, the local profiles $a(z)$ are not well defined; however, the excess quantities $a^s(z^s)$ are, since any ambiguities are “integrated out” over length scales that are large compared to the interfacial width. Such excess densities are defined for the internal energy, u^s , and species mass, ρ_α^s , with the total excess mass density $\rho^s = \sum_\alpha \rho_\alpha^s$. The excess entropy $s^s(z^s)$ represents a somewhat special case which will be discussed later. At equilibrium, these surface functions are related to one another through interfacial versions of the Euler and Gibbs–Duhem relations, which, for a two-component system, are given by

$$u^s = Ts^s + \gamma + \phi\rho_1^s + \mu_2\rho^s \quad [2a]$$

$$0 = s^s dT + d\gamma + \rho_1^s d\phi + \rho^s d\mu_2. \quad [2b]$$

We have chosen to write Eq. 2 in terms of the excess total mass density, $\rho^s = \rho_1^s + \rho_2^s$, and the difference in species chemical potentials, $\phi = \mu_1 - \mu_2$, as there are certain practical advantages associated with this representation; more discussion on this point is provided in *Materials and Methods*. Of course, other choices are possible (1, 4), and the resulting equations are equivalent by construction. Regardless of the specific form, further

manipulation of Eq. 2 leads to the celebrated Clapeyron and Gibbs adsorption equations that are the foundation of interfacial thermodynamics (1).

The Gibbs formulation reveals profound connections between “ambiguous” excess densities (which depend on the position of the dividing surface) and nonambiguous intensive quantities (which do not). Furthermore, the fundamental relationships themselves are insensitive to the position of the interface; this is perfectly natural for a macroscopic theory, as the details of the interface can only be resolved microscopically. In fact, one may view it as a requirement that any macroscopic thermodynamics of interfaces (equilibrium or otherwise) should rest on relationships that are valid regardless of the precise position of the surface. This insight has recently been used to develop interfacial thermodynamics in the formalism of gauge transformations (4, 25, 26), which are here identified as small changes in the location of the dividing surface. The “gauge” is the specific choice of z^s , and a gauge transformation $z^s \rightarrow z^s + l$ displaces the dividing surface by a small distance l normal to the interface toward phase II. As a result, the extensive densities are modified according to $a^s \rightarrow a^s + l\Delta a$, where Δa is the difference (or “jump”) between the bulk phase densities $\Delta a = a^I - a^{II}$ extrapolated to the interface. Since the variations in the bulk phase densities under nonequilibrium conditions are small compared to the gradients at the interface, we take the density jumps as independent of z^s (here and throughout the paper).

A gauge transformation of the interfacial Gibbs–Duhem and Euler equations reveals that these relations are only gauge invariant if we have $0 = \Delta s dT + \sum_{\alpha} \Delta \rho_{\alpha} d\mu_{\alpha}$ and $\Delta u = T\Delta s + \sum_{\alpha} \mu_{\alpha} \Delta \rho_{\alpha}$. By taking conditions of constant temperature and/or chemical potential(s), the Clapeyron and Gibbs adsorption equation(s) are immediately recovered. These results are typically reached by imposing the conditions of equilibrium, that is, constancy of the intensive variables (temperature, pressure, and chemical potentials) throughout the system (1). However, we see here that the same fundamental formulas can be obtained from a quite different (although still physically motivated) perspective, which does not explicitly require global equilibrium. This suggests that a nonequilibrium thermodynamics of interfaces might be established on the same grounds.

Local Equilibrium Theory of Interfaces

As discussed earlier, a theory of interfacial transport as powerful as that of bulk transport requires a local equilibrium assumption. We now examine the nature and implications of this assumption through the lens of gauge invariance described above. We begin by providing a brief but essential review of the theory developed in earlier works (4, 25–27) and then discuss how the underlying local equilibrium hypothesis may be tested in multicomponent systems. In this paper, we deal only with binary systems, and so will focus on the two-component case; the generalization to an arbitrary number of components is available elsewhere (4). A visualization of the system of interest is shown in Fig. 1A.

Theoretical Review. To begin, one hypothesizes nonequilibrium versions of the Euler and Gibbs–Duhem equations,

$$u^s = T^s s^s + \gamma + \phi^s \rho_1^s + \mu_2^s \rho^s \quad [3a]$$

$$0 = s^s dT^s + d\gamma + \rho_1^s d\phi^s + \rho^s d\mu_2^s. \quad [3b]$$

Note the subtle difference between Eqs. 2 and 3: The intensive quantities in the latter are associated specifically with the interface,

but are still gauge invariant. We now require that Eq. 3 remain valid after a gauge transformation, and therefore arrive at nonequilibrium versions of the Clapeyron equations,

$$\frac{\Delta \rho_1}{\Delta \rho} = - \left(\frac{\partial \mu_2^s}{\partial \phi^s} \right)_{T^s} \quad [4a]$$

$$\frac{\Delta s}{\Delta \rho} = - \left(\frac{\partial \mu_2^s}{\partial T^s} \right)_{\phi^s} \quad [4b]$$

$$\frac{\Delta u}{\Delta \rho} = \mu_2^s - T^s \left(\frac{\partial \mu_2^s}{\partial T^s} \right)_{\phi^s} - \phi^s \left(\frac{\partial \mu_2^s}{\partial \phi^s} \right)_{T^s}. \quad [4c]$$

Similarly, we can obtain nonequilibrium versions of the generalized Gibbs adsorption equation(s),

$$\Upsilon_1 \equiv \rho_1^s - \rho^s \frac{\Delta \rho_1}{\Delta \rho} = - \left(\frac{\partial \gamma}{\partial \phi^s} \right)_{T^s} \quad [5a]$$

$$\Upsilon_s \equiv s^s - \rho^s \frac{\Delta s}{\Delta \rho} = - \left(\frac{\partial \gamma}{\partial T^s} \right)_{\phi^s} \quad [5b]$$

$$\Upsilon_u \equiv u^s - \rho^s \frac{\Delta u}{\Delta \rho} = \gamma - T^s \left(\frac{\partial \gamma}{\partial T^s} \right)_{\phi^s} - \phi^s \left(\frac{\partial \gamma}{\partial \phi^s} \right)_{T^s}, \quad [5c]$$

where we have defined the relative adsorptions Υ_1 , Υ_s , and Υ_u of species mass, entropy, and internal energy, respectively.

In writing Eqs. 3–5, we have introduced gauge-invariant nonequilibrium intensive variables for the interface; specifically, the interfacial temperature, T^s , and chemical potentials, ϕ^s and μ_2^s . However, in practical situations, it is not immediately clear how to assign these values. In the bulk, it is straightforward to identify local temperatures and chemical potentials on the basis of local equilibrium: One has recourse to equilibrium statistical mechanics, so the temperature can be related to the kinetic energy and mass density profiles, while chemical potentials can be obtained, for instance, from particle insertion methods (28). This strategy is not applicable at interfaces away from equilibrium, for two reasons. First, one must assume that the local equilibrium assumption holds for the interfacial region in order to use such statistical mechanical relations. Since this is the very assumption we aim to evaluate, this is not acceptable for our purposes. Second, the results of such calculations are profiles of the apparent temperatures and chemical potentials through the interfacial region. However, the profiles can vary rapidly through this region, leading to the macroscopic “jumps” mentioned in the Introduction (Fig. 1B and C). As a result, any resulting values of the interfacial intensive variables would be gauge dependent, which is not permissible for a macroscopic thermodynamic description.

To address the difficulty of assigning intensive variables to the interface, several authors (25, 29) have suggested using the surface tension as an interfacial “thermometer.” The essential insight is that an interface in local equilibrium should obey not only interfacial Euler and Gibbs–Duhem relations (Eq. 3) but also the equilibrium equations of state. Concretely, the nonequilibrium surface tension, γ , can be directly measured in molecular simulations and does not depend on the specific choice of the dividing surface. Thus, for a one-component system, the equilibrium equation of state $\gamma(T)$ can be inverted to obtain a gauge-invariant interfacial temperature, T^s . Similarly, the interfacial chemical potential can be obtained as $\mu^s = \mu(T^s)$, where $\mu(T)$ is another equilibrium equation of state. For multicomponent systems, more gauge-invariant variables and associated equilibrium equations of state

are needed, since additional chemical potentials must be assigned. In particular, for a two-phase system with k components, the Gibbs phase rule indicates that k such variables are needed. Note also that the necessary equations of state become k dimensional. Proper choices for these variables are not always obvious, but we are nevertheless able to obtain the desired intensive quantities of the interface for binary systems, as discussed later. Interfacial temperatures and chemical potential differences obtained in this manner are denoted T^{eos} and ϕ^{eos} , respectively.

Testing Local Equilibrium. Although we have identified a practical method for assigning temperature and chemical potential(s) to the interface under nonequilibrium scenarios, we have not yet verified the local equilibrium assumption on which the method depends. To do so, we must show that Eqs. 4 and 5 are consistent with the equilibrium equations of state used to obtain T^{eos} and ϕ^{eos} . Specifically, we note that Eq. 4 relates nonequilibrium density jump ratios (which are gauge invariant) to the equation of state $\mu_2^s(T^s, \phi^s)$, which is simply identified as the equilibrium function $\mu_2(T, \phi)$ under the local equilibrium assumption. The density jump ratios can be directly calculated from molecular simulations, and any two such values allow one (in principle) to solve numerically for the interfacial intensive quantities via the equilibrium equation of state $\mu_2(T, \phi)$. These values are denoted T^{coex} and ϕ^{coex} , as they reflect the changes in bulk properties at the interface due to phase coexistence.

Analogous to the Clapeyron relations, Eq. 5 relates nonequilibrium gauge-invariant surface excess densities to the equation of state $\gamma(T^s, \phi^s)$, which is again taken as equivalent to the equilibrium equation of state, $\gamma(T, \phi)$. The relative adsorptions for species mass and internal energy are available via simulation, so interfacial intensive variables may once again be obtained and are denoted T^{stru} and ϕ^{stru} . This label highlights the fact that, in the equimolar gauge, the surface tension (which characterizes the mechanical structure of the interface) acts as a thermodynamic potential (29).

Note that the relative adsorption of entropy cannot be calculated without assuming, a priori, the local equilibrium of the interface, since determining the excess entropy density requires one to specify a local entropy profile throughout the interfacial region. However, the entropy cannot be measured except in reference to other thermodynamic quantities through the Euler equation. In doing so, we tacitly assume that the Euler relation itself is valid in the interfacial region, so that any demonstration of local equilibrium becomes a circular argument. This point has been discussed in greater detail elsewhere (29). For these reasons, the excess entropy—even in equilibrium systems—must be inferred from the interfacial Euler relation, Eq. 2a (or Eq. 3a), rather than through an integration of any local profile as in Eq. 1. Thus, Eq. 5b has the character of a definition rather than a requirement. It is this definition of a gauge-transformable excess entropy density that allows for nonequilibrium versions of the fundamental thermodynamic relations, Eq. 3. As a result, we must use Eqs. 5a and 5c to determine T^{stru} and ϕ^{stru} , in contrast to T^{coex} and ϕ^{coex} , for which three pairs of equations could be chosen (compare Eq. 4).

In total, we have identified three separate methods of obtaining intensive thermodynamic quantities for the interface in nonequilibrium systems: 1) using equations of state for interfacial variables as “thermometers,” 2) using observed jump ratios to solve Eq. 4, and 3) using measured relative adsorptions to solve Eq. 5. If local equilibrium were valid at the interface, then the Euler and Gibbs–Duhem, as well as equilibrium equations of state, would apply away from equilibrium. As a result, all three sets of values

(T, ϕ) should be equivalent within statistical error. We rely on high-precision MD simulations, as described below, to test the local equilibrium hypothesis for interfaces. We first identify appropriate interfacial variables and then parameterize the various equilibrium equations of state needed for the methods introduced above. Then, we perform extensive NEMD simulations at steady state with both energy and mass flux (including coupling between the two) and demonstrate the validity of the local equilibrium hypothesis for interfaces in binary systems.

Equilibrium Systems

Applying the theory of local interfacial equilibrium to any particular system of interest requires two types of information: 1) knowledge of the equilibrium equations of state and 2) identification of suitable interfacial variables that can be used away from equilibrium. We obtain this information from equilibrium MD simulations performed with extremely high precision. In particular, we simulate a binary system of Lennard-Jones particles comprising coexisting liquid and vapor phases. We directly specify the values of T and ϕ during the simulations (see *Materials and Methods*), which uniquely and completely determine the thermodynamic state of the system per the Gibbs phase rule (8). The two chemical species have different interaction energies, which lead to different critical temperatures in their respective pure systems. Thus, we may say that one component is more “liquid-like” and the other is more “gas-like.” A visual representation of the system is shown in Fig. 1A.

From the right-hand sides of Eqs. 4 and 5, we see that we must first determine the equations of state $\mu_2(T, \phi)$ and $\gamma(T, \phi)$ as well as their derivatives at constant T and ϕ . The values of μ_2 are calculated via the Widom insertion method, while those of γ are determined from the negative of the excess tangential pressure, which does not depend on the choice of dividing surface (see *Materials and Methods*). A total of 42 equilibrium simulations were performed with $0.0 \leq \phi \leq 1.5$ and $0.6 \leq T \leq 0.85$, where the quantities have been made dimensionless by the Lennard-Jones characteristic parameters. The highest temperature is close to the critical point of the gas-like species, while the lowest temperature brings the system close to the liquid/solid coexistence region of the liquid-like species. Meanwhile, the values of ϕ lead to mole fractions of the liquid-like component in the range of 0.10 to 0.97 in the liquid. In short, the choice of parameters explores a large area of thermodynamic space while still ensuring that the system is well mixed and within the liquid–vapor coexistence region. The resulting equations of state, $\mu_2(T, \phi)$ and $\gamma(T, \phi)$, and their gradients, are fit with smoothing bivariate cubic splines (Fig. 2A and B), which can be used along with the density profiles $\rho(z)$, $\rho_1(z)$, and $u(z)$ to solve Eqs. 4 and 5.

Next, we must identify two gauge-invariant interfacial quantities that can be used to determine $(T^{\text{eos}}, \phi^{\text{eos}})$. The surface tension is one obvious choice, as it is the only intensive quantity with a mechanical definition valid in both equilibrium and nonequilibrium situations. For an additional interfacial variable, several authors (4, 27) have suggested the relative adsorption of species, Υ_1 , defined in Eq. 5a. However, for this particular system, the adsorptions are nonmonotonic functions of ϕ , so that a given set of values (γ, Υ_1) does not always map to a unique thermodynamic state (T, ϕ) . The jump ratios appearing on the left-hand side of Eq. 4 provide a more useful choice, with the species mass jump ratio $\Delta\rho_1/\Delta\rho$ being the easiest to obtain with high accuracy (Fig. 2C). These variables are indeed monotonic functions of T and ϕ , and therefore allow $(T^{\text{eos}}, \phi^{\text{eos}})$ to be determined unambiguously, as illustrated in Fig. 2D.

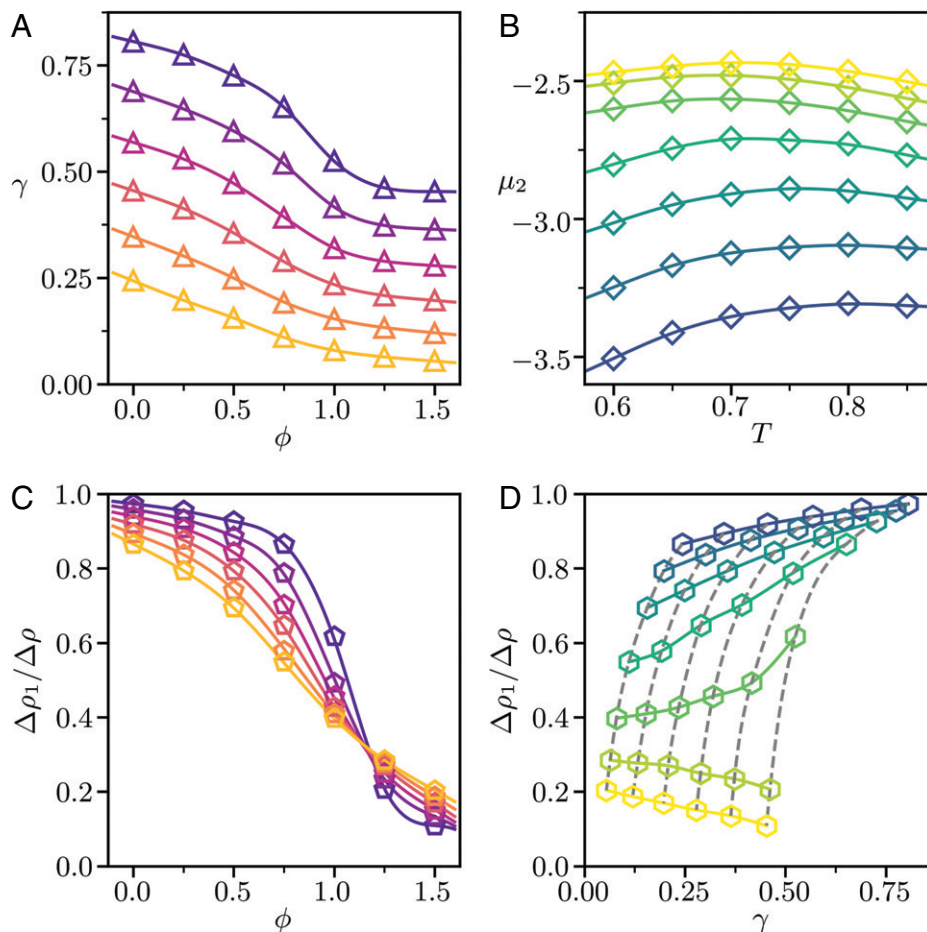


Fig. 2. Equations of state for equilibrium systems. (A) Surface tension, $\gamma(T, \phi)$. Colors from purple to orange indicate increasing temperature, T . The lines are isotherms of the fitted bivariate spline. (B) Chemical potential of the gas-like species, $\mu_2(T, \phi)$. Colors from blue to yellow indicate increasing chemical potential difference, ϕ . The lines are points of constant ϕ of the fitted bivariate spline. (C) Interfacial jump ratio $\Delta\rho_1/\Delta\rho$. As in A, the lines are isotherms of the fitted bivariate spline. (D) $\Delta\rho_1/\Delta\rho$ vs. γ . The colored lines indicate constant ϕ , while the grey dashed lines indicate constant T .

Before continuing, we emphasize again that the chosen interfacial variables must be gauge invariant. Since the bulk densities are constant at equilibrium, the jump ratio $\Delta\rho_1/\Delta\rho$ trivially satisfies this condition under these circumstances. However, the bulk densities generally vary with position when out of equilibrium, so that the jumps must be calculated from the bulk density profiles extrapolated to the interface, as mentioned in the previous section. As a result, these variables are not technically gauge invariant, since the profiles must be extrapolated to a specific choice of the dividing surface, z^s . This is of no practical concern, however, because the density gradients in the bulk are generally much smaller than those at the interface, so that variations in $\Delta\rho_1/\Delta\rho$ associated with gauge transformations (say, between the equimolar and equienergetic gauges) are comparable with (or smaller than) the statistical uncertainty in the values themselves. The only scenarios in which the gauge-dependence is not negligible are at high temperatures near the critical point of the gas-like species, where the interfacial width becomes very large. Of course, we do not expect the theory to remain valid near a critical point, since these states are essentially “nonthermodynamic” in that the fluctuations dominate over the means, rather than the other way around (30). Since $\Delta\rho_1/\Delta\rho$ is approximately gauge invariant for relevant systems, we adopt this as the second interfacial variable without further reservations and calculate its value by extrapolating to the equimolar gauge ($\rho_s = 0$). This choice of gauge is essentially arbitrary, but is consistent with the form of Eq. 5. Finally, we determine the equation of state $[\Delta\rho_1/\Delta\rho](T, \phi)$

from the equilibrium simulation data and fit the results with a smoothing bivariate cubic spline, as with the other equations of state detailed above (Fig. 2C).

Nonequilibrium Systems

Having laid the necessary foundations, we now conduct an array of NEMD simulations to test the local equilibrium assumption. We consider steady-state nonequilibrium systems where energy or species mass flux are driven by a gradient in T or ϕ , respectively (see *Materials and Methods*). Note, however, that, in each case, both energy and mass flux occur on account of cross-effects (4, 7), which couple these fluxes.

It should be appreciated that, although we only conduct simulations at steady state, this is not required by the theory presented above. One should only ensure that the time/length scales associated with the evolution of the thermodynamic fluxes/forces is longer than the time/length associated with local thermalization (i.e., collision frequency, density gradient, etc.). This same criterion applies also in the case of bulk transport and is therefore not unique to the present theory. Rather, the focus on stationary states is a matter of computational practicality. In order to accurately measure surface excess densities and jumps, one must be able to survey a large enough area of the surface for a long enough time so that fluctuations may be “averaged out.” When the interface is moving (as in unsteady conditions), such calculations are greatly complicated, as it becomes difficult to distinguish between

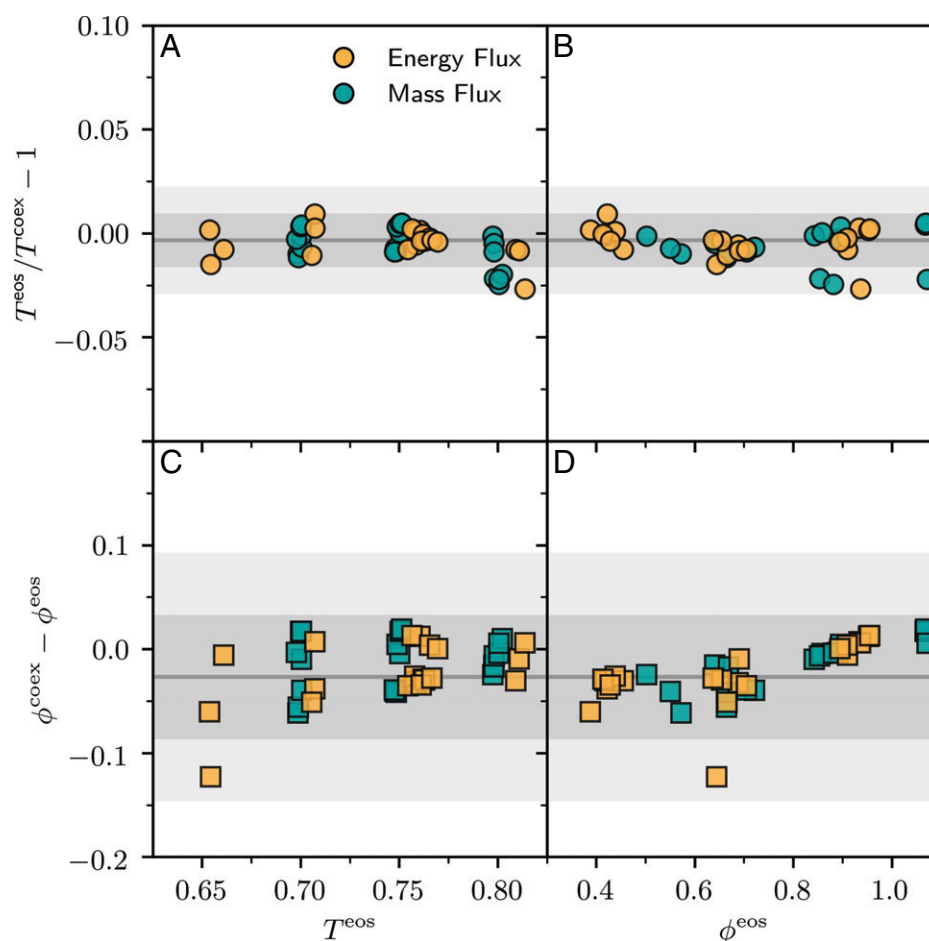


Fig. 3. (A) Relative error between interfacial temperatures obtained from equilibrium equations of state, T^{eos} , and from Eq. 4, T^{coex} , as a function of T^{eos} . The dark and light shaded regions represent 1 and 2 SDs, respectively, of the equilibrium data. Each data point represents a different nonequilibrium simulation with unique parameters (see *Materials and Methods*). (B) The same data as in A, but plotted against ϕ^{eos} . (C) Absolute error between interfacial chemical potential differences obtained from equilibrium equations of state, ϕ^{eos} , and from Eq. 4, ϕ^{coex} , as a function of T^{eos} . As in A, the shaded regions represent the spread of the equilibrium data. (D) The same data as in C, but plotted against ϕ^{eos} . In all cases, error bars are approximately the size of the data points.

fluctuation and evolution. Of course, it is indeed possible to simulate dynamic surface phenomena (31, 32), but the high precision required for a test of local equilibrium (including the calculation of chemical potentials) makes this a major computational challenge in the present work.

Given the small length and time scales associated with molecular simulations, the gradients and fluxes observed here are, in fact, quite extraordinary. For instance, if one assumes Argon-like Lennard-Jones parameters (33), the temperature gradients are on the order of 10^6 K/m, and the species mass velocities are on the order of 1 m/s. Thus, the present analysis, in fact, provides a stringent test of the local equilibrium hypothesis, dealing with interfaces in systems far from equilibrium.

Clapeyron Equations. As outlined earlier, Eq. 4 is tested by calculating the density jump ratios directly from the simulation data and then solving for $(T^{\text{coex}}, \phi^{\text{coex}})$ through the equilibrium equation of state $\mu_2(T, \phi)$ and its derivatives (Fig. 2B). The resulting values should be consistent with $(T^{\text{eos}}, \phi^{\text{eos}})$. In practice, only two of Eqs. 4a–4c are necessary to solve for the thermodynamic state of the interface, but all three such combinations must yield consistent results to ensure the gauge invariance of Eq. 3. Satisfyingly, we have found that all three associated values of $(T^{\text{coex}}, \phi^{\text{coex}})$ are essentially identical. Thus, we focus our attention those quantities obtained from the most easily calculated

set of jump ratios, $\Delta\rho_1/\Delta\rho$ and $\Delta u/\Delta\rho$. A direct comparison with the other combinations is provided in *SI Appendix*.

The results of our analysis are shown in Fig. 3, with each data point corresponding to an individual NEMD simulation with unique parameters (see *Materials and Methods*). We consider the relative error for interfacial temperatures, and the absolute error for chemical potential differences. Such comparisons are chosen since the temperature is strictly positive, while the chemical potential difference can approach zero (and become negative), thereby resulting in misleadingly large relative errors. As expected, there is considerable scatter in the data, which exceeds that observed for one-component systems (29). Indeed, the binary systems are more challenging to handle numerically owing to the additional thermodynamic variable. Even on a fundamental level, the extra degree of freedom allows for a much greater range of fluctuations in the thermodynamic state of the interface.

To properly interpret this error, we conduct the same analysis on the equilibrium systems discussed above; in these systems, Eq. 4 is exact, so the statistical variations in these cases set a reasonable benchmark for validating the nonequilibrium applicability of the Clapeyron equations. The ranges of 1 and 2 SDs of the equilibrium data are shown as gray shaded regions in Fig. 3. Almost all nonequilibrium data fall within one such SD, and the mean errors are not statistically distinguishable from those of the equilibrium systems. In summary, the accuracy of Eq. 4 is not appreciably

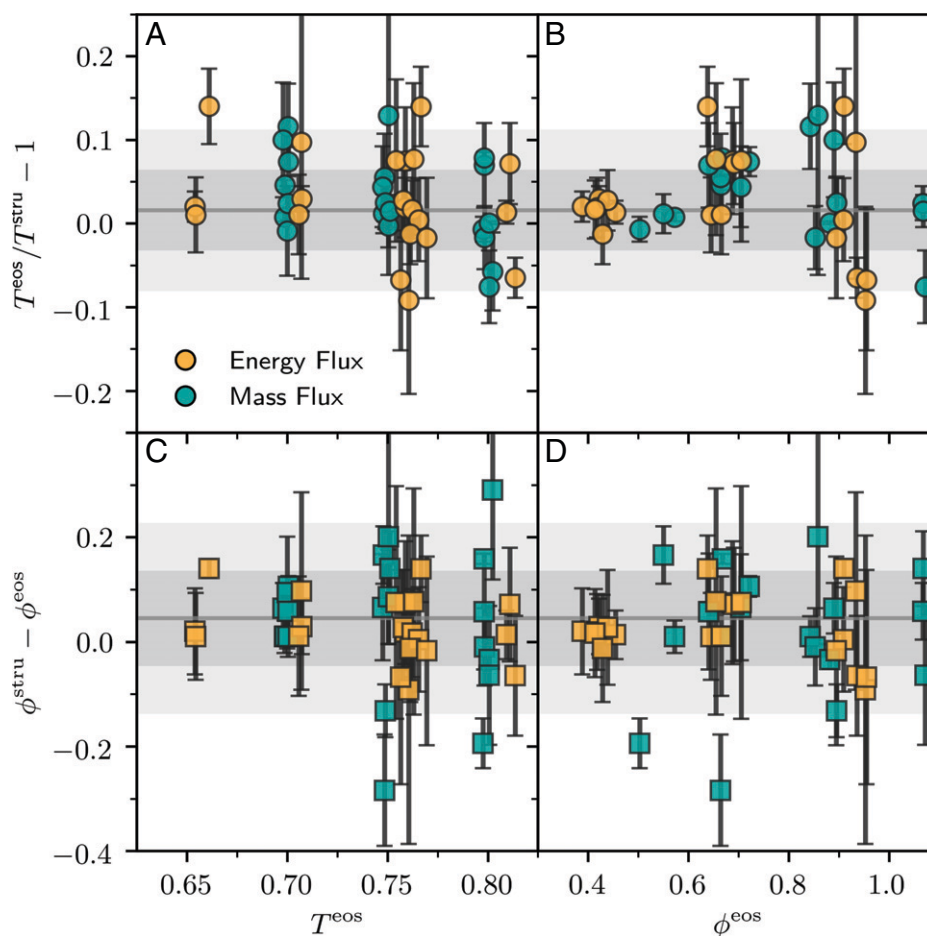


Fig. 4. (A) Relative error between interfacial temperatures obtained from equilibrium equations of state, T^{eos} , and from Eq. 4, T^{coex} , as a function of T^{eos} . The dark and light shaded regions represent 1 and 2 SDs, respectively, of the equilibrium data. Each data point represents a different nonequilibrium simulation with unique parameters (see *Materials and Methods*). (B) The same data as in A, but plotted against ϕ^{eos} . (C) Absolute error between interfacial potential differences obtained from equilibrium equations of state, ϕ^{eos} , and from Eq. 4, ϕ^{coex} , as a function of T^{eos} . As in A, the shaded regions represent the spread of the equilibrium data. (D) The same data as in C, but plotted against ϕ^{eos} .

diminished in the presence of energy and/or mass flux, supporting the local equilibrium hypothesis.

Importantly, we find that these results show no dependence on either T^{eos} or ϕ^{eos} . Likewise, the results do not depend on the magnitude (or sign) of the fluxes (*SI Appendix*), which might indicate a restricted range of validity. We therefore conclude that the Clapeyron Eq. 4 may indeed be generalized to interfaces in nonequilibrium systems.

Gibbs Adsorption Equations. We now test Eq. 5 by calculating the excess species mass and energy densities in the equimolar gauge ($\rho^s = 0$) and solving for $(T^{\text{stru}}, \phi^{\text{stru}})$ through the equilibrium equation of state $\gamma(T, \phi)$ and its derivatives (Fig. 2A). As mentioned earlier (and in contrast with the earlier test[s] of Eq. 4), only one of the three possible pairs of Eq. 5 may be chosen to solve for the thermodynamic state of the interface, as it is not possible to define a local entropy profile $s(z)$ in the interfacial region without assuming local interfacial equilibrium a priori (29).

The results of this analysis are shown in Fig. 4, in the same format as that adopted for the earlier analysis of the Clapeyron equations. The error in the data is larger, both in equilibrium and nonequilibrium systems, owing to the highly fluctuating nature of the interface, which makes the excess densities difficult to determine with high precision. Nevertheless, the nonequilibrium systems show no greater uncertainty or error than the equilibrium systems, which is all that can be expected when testing the local

equilibrium hypothesis. As with the earlier test of Eq. 4, there is no meaningful dependence of the error on either T^{eos} or ϕ^{eos} , or the magnitude of the fluxes (*SI Appendix*). It is therefore clear that the generalized Gibbs adsorption equations, Eq. 5, are also valid out of equilibrium.

Discussion

The distributions of the data in Figs. 3 and 4 are shown as box-and-whisker plots in Fig. 5. The data for the nonequilibrium systems are generally comparable to those at equilibrium, in terms of both the width of the distributions and any deviation from zero error. The similarity in these distributions points to the validity of the local equilibrium description for the interface in nonequilibrium settings.

For comparison, we have also included the distribution of temperatures and chemical potential differences obtained from extrapolating the bulk profiles in the liquid or vapor to the equimolar gauge. Although these data often appear much closer to zero and exhibit less scatter than the coexistence or structural intensive variable values, they are highly dependent on the size of the jumps in intensive variables (compare Fig. 1 B and C). For instance, in the systems studied here, the largest jumps occur in the temperature profile under energy flux. For such systems, the temperatures extracted from the vapor-phase profile deviate significantly from the interfacial temperature; in these situations,

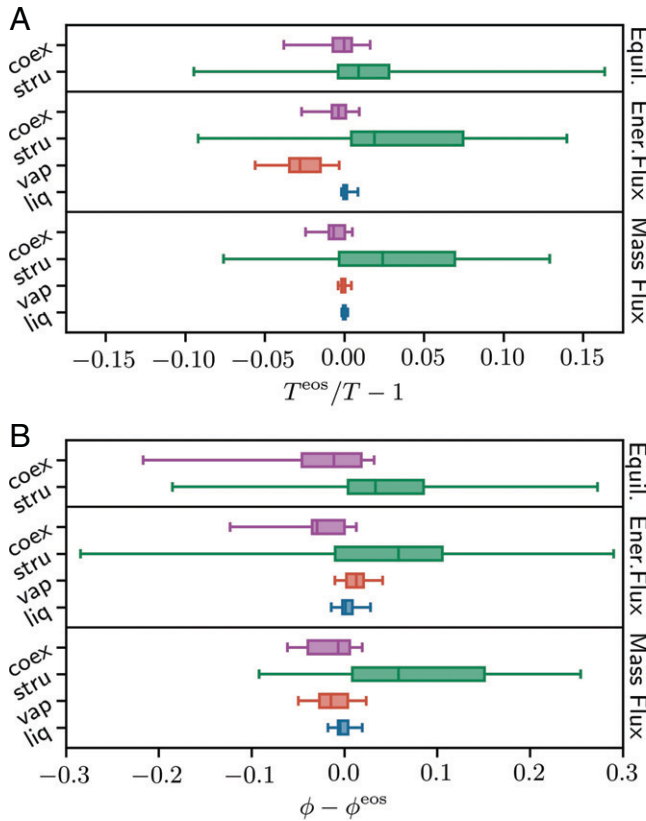


Fig. 5. Box-and-whisker representation of the data in Figs. 3 (coex) and 4 (stru) for (A) temperature and (B) chemical potential difference. Also shown are the apparent interfacial values of (T, ϕ) determined by extrapolating the bulk temperature and chemical potential profiles of the vapor (vap) and liquid (liq) phases to the interface.

the relatively small error actually leads to the conclusion that such a method of choosing the interfacial temperature is incorrect.

In most of the other simulated systems, the interfacial jumps are fairly small, so the deviations of the liquid/vapor intensive variables from the “true” interfacial ones are not detectable (although this is not required for the current theory). However, the small jumps observed here must be understood as special cases: Since the entropy production at the interface is usually taken as proportional to the squared magnitude of the jumps (4), the system will arrange itself so as to minimize these jumps (and hence entropy production), given the steady-state conditions (7). Meanwhile, in complex, unsteady flows, one cannot assume that the jumps are small. Thus, the use of bulk information for defining intensive thermodynamic values of the interface has limited validity, as was demonstrated earlier in pure systems (29). On the other hand, the use of equilibrium equations of state (i.e., the calculation of T^{eos} and ϕ^{eos}) is evidently valid in all circumstances, regardless of the magnitude of the temperature or chemical potential jumps. Taken together, these results serve to establish the interfacial “thermometer” method (25) as a powerful tool for analyzing transport in heterogeneous systems.

Having established the validity of the local equilibrium hypothesis for interfaces in nonequilibrium conditions, one may now formulate thermodynamically consistent constitutive relations by the usual procedure of demanding nonnegative entropy production (4, 7). Similarly, the coefficients appearing in these equations can be determined through an analysis of the data collected here. However, although the governing transport equations are universal in form and content, the transport coefficients are phenomenological and system specific. Therefore, these quantities are not particularly relevant to the present work, as we have

primarily concerned ourselves with the more general aspects of interfacial transport. Nevertheless, interested readers may obtain and analyze the simulation data at their convenience (see *Data Availability*).

Conclusion

Linear irreversible thermodynamics (4, 7) provides a foundation for the study of a wide array of transport phenomena. For bulk systems, the theory is so successful that it has become a key component of standard pedagogy in physics, biology, engineering, and elsewhere. Extending these concepts to interfaces has proved challenging, owing to the existence of macroscopic discontinuities in the intensive variable profiles (e.g., temperature jumps), which complicate the underlying local equilibrium assumption. Moreover, the popular phase-field or diffuse interface models cannot assess the validity of such an assumption.

Here, we have discussed and evaluated a local equilibrium theory of multicomponent interfaces in the sharp interface framework that is based on the concept of gauge transformations. Simply put, the macroscopic thermodynamics cannot depend on microscopic changes in the interface position. The consequences of this postulate provide methods to test the local equilibrium hypothesis, which is shown to be applicable through extensive MD simulations. Furthermore, we have established a reliable procedure for determining nonequilibrium interfacial temperatures and chemical potentials on the basis of equilibrium equations of state. Proper assignment of these intensive variables is crucial for developing interfacial constitutive relations, and for accurate calculation of the associated transport coefficients. In summary, the formulation of local equilibrium at interfaces presented here provides a flexible and thermodynamically rigorous method for modeling interfacial transport.

Materials and Methods

We simulate a binary mixture of particles with mass m interacting via a smoothed Lennard-Jones spline potential,

$$\phi_{\alpha\beta}(r) = \begin{cases} 4\epsilon_{\alpha\beta} \left[\left(\frac{\sigma_{\alpha\beta}}{r} \right)^{12} - \left(\frac{\sigma_{\alpha\beta}}{r} \right)^6 \right] & \text{if } 0 < r < r_s \\ \epsilon_{\alpha\beta} \left[\zeta_1 (r - r_c)^3 + \zeta_2 (r - r_c)^2 \right] & \text{if } r_s \leq r \leq r_c \\ 0 & \text{otherwise,} \end{cases} \quad [6]$$

where r is the interparticle distance, and $\alpha, \beta \in \{1, 2\}$ denote the particle species. Here we use the parameters $\sigma_{11} = \sigma_{22} = \sigma_{12} = \sigma$ and $\epsilon_{11} = \epsilon, \epsilon_{22} = \epsilon_{12} = 0.8\epsilon$. The cutoff radius is chosen as $r_c = 2.5\sigma$, and the parameters $r_s = (48/67)r_c, \zeta_1 = 0.099194\sigma^{-3}, \zeta_2 = -0.16346\sigma^{-2}$ are assigned so that the potential and its first derivative (i.e., the force) are continuous and vanish at r_c . This same model has been used in several other investigations of thermodynamics and transport in binary systems (34–38). All physical quantities are made dimensionless with $m, \sigma, \epsilon, \epsilon/k_B$, and $\tau = (m\sigma^2/\epsilon)^{1/2}$ as the units of mass, length, energy, temperature, and time, respectively.

All systems consist of 16,000 particles placed in a simulation box with x, y, z dimensions $L_x = L_y = 20$ and $L_z = 200$. We use periodic boundary conditions in the x and y directions and place walls at $z = 0$ and $z = L_z$. The left wall is designed to encourage nonpreferential wetting of the liquid phase. Specifically, at a distance z from the left wall, particles are subject to a 10–4 Lennard-Jones spline potential (39),

$$\phi_w(z) = \begin{cases} \frac{8\pi\epsilon}{5} \left[\frac{2}{5} \left(\frac{\sigma}{z} \right)^{10} - \left(\frac{\sigma}{z} \right)^4 \right] & \text{if } 0 < z < z_s \\ \epsilon_w \left[\omega_1 (z - z_c)^3 + \omega_2 (z - z_c)^2 \right] & \text{if } z_s \leq z \leq z_c \\ 0 & \text{otherwise,} \end{cases} \quad [7]$$

where, by analogy with Eq. 6, we choose $\epsilon_w = \epsilon/2, z_c = r_c$, and $z_s = r_s$. Likewise, the parameters $\omega_1 = -0.603715$ and $\omega_2 = -1.388096$ were chosen

to ensure that the energy and force are continuous and vanish at z_c . To further ensure that the liquid remained at the bottom of the simulation cell, we applied a small force, in the z direction, of -0.005 to all particles within 5.0 particle diameters of the left wall and set the total momentum of the particles within this region to zero every 2,000 time steps (rescaling particle velocities to leave kinetic energy unchanged). This wall alters the structure of the nearby fluid, creating a layering effect. However, the oscillations in the associated distribution functions $\rho_\alpha(z)$ disappear at distances greater than $z \approx 5\sigma$ (40), which is considerably smaller than the size of the thermodynamic bath (see below). The right wall is implemented as a hard surface which reflects all particles that move beyond $z = L_z$. The reflection is specular (elastic) in the z dimension and diffuse in the x and y dimensions so that the wall also acts as a thermostat (41). Since the interactions between the particles and the right wall are purely repulsive, the adjoining phase is maintained as a vapor.

Near the walls, we implement thermodynamic baths which maintain constant temperature, T , and chemical potential difference, ϕ , in the spirit of the dual control volume method (42). The left bath encompasses the region $0 < z < 10$ and is thermostated using the canonical sampling by velocity rescaling (CSVR) method (43). This method chooses velocity scaling factors based on a stochastic evolution of the kinetic energy. These auxiliary dynamics depend on the number of degrees of freedom, which can vary within the specified bath region; thus the targeted kinetic energy is updated at each time step as particles drift in and out of the bath. A time constant of 0.1 was used for this algorithm. To maintain constant ϕ , we perform Monte Carlo particle identity swaps in the semigrand canonical ensemble (44–46). The acceptance criteria for these identity changes depend on (among other things) the number of particles in the bath region, which is measured prior to each attempted swap.

The right thermodynamic bath acts on the region $L_z - 10 < z < L_z$, occupied by the vapor phase. We maintain the region at constant temperature using the Andersen thermostat (47) with a characteristic time of 0.1. We use a different thermostat in the right bath because we found that the CSVR algorithm often leads to large velocity changes and numerical instabilities due to the low density of the vapor. Moreover, the Andersen method mimics rare collision events, making it a physically appealing choice for the vapor phase. To maintain constant chemical potential difference in the right bath, we again apply the Monte Carlo approach previously described for the left bath.

Using the thermodynamic baths described above, one can more directly control the system. For instance, we can induce a species mass flux by choosing different values of ϕ for each bath. Likewise, the system can be subjected to an energy flux by choosing different values of T in each bath. One key advantage of the direct control over ϕ is that coupled energy/mass transport is possible under a temperature gradient. Without performing particle identity swaps, the steady state of such a system will not experience any species mass flux, thus limiting the breadth of transport processes that can be studied, as was the case in previous computational investigations of these systems. From a theoretical point of view, direct control of two intensive variables is greatly preferred, since Eqs. 4 and 5 deal with derivatives of various equations of state with respect to one intensive variable while holding the other constant. While this could be done with the use of grand canonical Monte Carlo methods (46), these algorithms are much less efficient than the semigrand Monte Carlo, since they rely on particle insertions, which are rarely accepted in condensed phases.

While the algorithms implemented here do indeed maintain temperature and chemical potential difference with great accuracy, we have made no effort to ensure that they rigorously reproduce the semigrand canonical distribution. However, this is not important for our purposes, as these algorithms act only within relatively small regions of the simulation cell which are far removed from the interface. Indeed, the position of the interface is roughly $z_s \approx 30$ to 50σ so that there is 20 to 40σ of bulk liquid between the left bath and the interface. Outside of the baths, the system evolves according to Hamiltonian dynamics, free from the influence of any thermostats or Monte Carlo moves. Thus, in the region of physical interest (and a great deal of the surrounding volume), mass, species, energy, and momentum are locally conserved, which provides the foundation for a nonequilibrium thermodynamic description of the system.

Particle coordinates $\{\mathbf{r}_i(t)\}$ are evolved in time according to Newton's equations of motion using the Velocity-Verlet algorithm (46) with a time step of $\delta t = 0.0005\tau$. Owing to the slow diffusion dynamics in the liquid phase, the systems require extensive preparation to ensure equilibrium or steady-state

conditions. In particular, equilibrium and nonequilibrium systems were preconditioned for 150 to $250 \times 10^6 \delta t$ and $250 \times 10^6 \delta t$, respectively, and we verified that energy flux, species mass flux, and species density profiles were constant (within statistical uncertainty) over the course of the simulations. Following the system preparation, production simulations of $250 \times 10^6 \delta t$ were performed, and the trajectories were analyzed as five separate chunks of $50 \times 10^6 \delta t$ to estimate statistical uncertainties, which are reported as 95% CIs unless otherwise noted.

To impose an energy flux in the systems, we set the right and left baths to the same chemical potential difference and different temperatures. To impose a species mass flux, the bath temperatures are kept identical, but the chemical potential differences are set to different values. In both of these scenarios, cross-effects occur: The temperature gradient induces a gradient in the chemical potential difference, and vice versa. Note, however, that the particles have equal mass so that the total mass flux is zero at steady state; that is, the barycentric reference frame is the same as the laboratory/wall reference. Parameters for the various simulations are shown in Table 1.

To analyze spatial variations in thermodynamic quantities, we divide the system into 400 slabs of thickness $\sigma/2$ in the z direction with the position of each layer $k \in \{1, 2, \dots, 400\}$ given by $z_k = k/2 - \sigma/4$. In each layer,

Table 1. Nonequilibrium simulation parameters (liquid/vapor thermostat temperatures and chemical potential differences)

Flux	Liquid temperature	Vapor temperature	Liquid ϕ	Vapor ϕ
Energy flux	0.65	0.95	0.5	0.5
	0.65	0.95	0.75	0.75
	0.65	0.95	1.00	1.00
	0.70	1.00	0.50	0.50
	0.70	1.00	0.75	0.75
	0.70	1.00	1.00	1.00
	0.75	0.95	0.50	0.50
	0.75	0.95	0.75	0.75
	0.75	0.95	1.00	1.00
	0.75	1.05	0.50	0.50
	0.75	1.05	0.75	0.75
	0.75	1.05	1.00	1.00
	0.75	1.15	0.50	0.50
	0.75	1.15	0.75	0.75
	0.75	1.15	1.00	1.00
	0.75	1.25	0.50	0.50
	0.75	1.25	0.75	0.75
	0.75	1.25	1.00	1.00
	0.80	1.10	0.50	0.50
	0.80	1.10	0.75	0.75
0.80	1.10	1.00	1.00	
Mass flux	0.70	0.70	0.25	1.00
	0.70	0.70	0.50	1.00
	0.70	0.70	0.50	1.25
	0.70	0.70	0.75	1.25
	0.70	0.70	0.75	1.50
	0.70	0.70	1.25	0.50
	0.70	0.70	1.25	0.75
	0.75	0.75	0.25	1.00
	0.75	0.75	0.50	1.00
	0.75	0.75	0.50	1.25
	0.75	0.75	0.75	1.25
	0.75	0.75	0.75	1.50
	0.75	0.75	1.25	0.50
	0.75	0.75	1.25	0.75
	0.80	0.80	0.25	1.00
	0.80	0.80	0.50	1.00
0.80	0.80	0.50	1.25	
0.80	0.80	0.75	1.25	
0.80	0.80	0.75	1.50	
0.80	0.80	1.25	0.50	
0.80	0.80	1.25	0.75	

we calculate, at every time step, the instantaneous species mass density, $\rho_{k,\alpha}(t) = (m/V_s) \sum_i \mathbb{1}_{ki,\alpha}(t)$ where m is the particle mass, $V_s = L_x L_y \sigma / 2$ is the slab volume, and $\mathbb{1}_{ki,\alpha}(t)$ is an indicator function: $\mathbb{1}_{ki,\alpha}(t) = 1$ if particle i is of species α and is in slab k at time t , and $\mathbb{1}_{ki,\alpha}(t) = 0$ otherwise. The total mass density is the sum over both species mass densities: $\rho_k(t) = \rho_{k,1}(t) + \rho_{k,2}(t)$. Similarly, we calculate the species momentum density $\mathbf{m}_{k,\alpha}(t) = (m/V_s) \sum_i \mathbb{1}_{ki,\alpha}(t) \mathbf{v}_i(t)$, where $\mathbf{v}_i(t) = \dot{\mathbf{r}}_i(t)$ is the velocity of particle i . Note that the species momentum density is equivalent to the species mass flux. The total momentum density follows as $\mathbf{m}_k(t) = \mathbf{m}_{k,1}(t) + \mathbf{m}_{k,2}(t)$. The average barycentric velocity in slab k is then given in terms of the time-averaged total momentum and total mass densities: $\bar{\mathbf{v}}_k = \bar{\mathbf{m}}_k / \bar{\rho}_k$, where \bar{a} is the time average of the quantity $a(t)$.

The instantaneous potential energy density is calculated as $\psi_k(t) = (1/2V_s) \sum_{i \neq j} \mathbb{1}_{ki}(t) \phi_{\alpha_i \beta_j}(r_{ij}(t))$, where α_i and β_j are the species of particles i and j , respectively, $r_{ij} = |\mathbf{r}_i(t) - \mathbf{r}_j(t)|$ is the distance between particles i and j , and $\mathbb{1}_{ki}(t)$ is a species-agnostic version of the indicator function defined earlier. As pointed out in previous literature (1,29) and discussed in detail in the main text (section *Diffuse Interfaces*), the definition of $\psi_k(t)$ is actually somewhat ambiguous: If interacting particles are in different slabs, how should the potential energy be partitioned between these slabs (or among any slabs in between)? Here, we choose to assign to each layer one-half of the interaction energy, as earlier analysis has indicated that systematic variations in the potential energy density associated with various partitioning schemes are much smaller than statistical uncertainties. Moreover, these subtleties are "integrated out" in our analysis of local equilibrium, so the precise choice should be unimportant.

The instantaneous nonconvected kinetic energy density is expressed as $\eta_k(t) = (m/2V_s) \sum_i \mathbb{1}_{ki}(t) [\mathbf{v}_i(t) - \bar{\mathbf{v}}_k]^2$. Since the barycentric velocity is not known prior to running the simulations, we instead calculate, at each time step, the instantaneous total kinetic energy, $\xi_k(t) = (m/2V_s) \sum_i \mathbb{1}_{ki}(t) \mathbf{v}_i^2(t)$. The time-averaged nonconvected kinetic energy (which is the quantity of interest for thermodynamic analysis) can then be expressed as $\bar{\eta}_k = \bar{\xi}_k - (1/2) \bar{\rho}_k \bar{\mathbf{v}}_k^2$ using the relationships given above. The total internal energy density profile is then obtained from $\bar{u}_k = \bar{\psi}_k + \bar{\eta}_k$.

The temperature profile is obtained from the kinetic energy and mass densities as $T(z_k) = (2m/3)(\bar{\eta}_k/\bar{\rho}_k)$. To compute the pressure, we calculate the instantaneous virial tensor $\boldsymbol{\nu}_k(t) = \sum_{i \neq j} \mathbb{1}_{ki}(t) \mathbf{r}_{ij} \mathbf{f}_{ij}$, where \mathbf{f}_{ij} is the force on particle i due to particle j . The pressure profile then follows as $p(z_k) = (2/3) \bar{\eta}_k + (1/6V_s) \text{Tr}(\bar{\boldsymbol{\nu}}_k)$. The surface tension is also expressed in terms of the virial tensor by evaluating the difference of normal and tangential components of the pressure: $\gamma = -(1/4L_x L_y) \sum_k [\text{Tr}(\bar{\boldsymbol{\nu}}_k) - 3\mathbf{n} \cdot \bar{\boldsymbol{\nu}}_k \cdot \mathbf{n}]$, where \mathbf{n} is a unit vector normal to the interface (i.e., in the z direction). Note that we only consider slabs in the neighborhood of the interface, as the pressure anisotropy vanishes in the bulk phases.

The chemical potentials in the system are expressed as sums of ideal and excess parts: $\mu_{\alpha}(z_k) = \mu_{\alpha,k} = \mu_{\alpha,k}^{\text{id}} + \mu_{\alpha,k}^{\text{ex}}$. The ideal contribution is $\mu_{\alpha}^{\text{id}} = -(3/2)T \ln T + T \ln \rho_{\alpha}$. Note that the first term formally involves the thermal de Broglie wavelength, which includes the Planck constant, h . Unfortunately, it is not possible to determine the value of this constant in reduced units without specifying values for m , σ , and ϵ . However, in the classical system considered here, the Planck constant merely sets a reference entropy, S_0 . Although a change in the reference entropy changes the numerical value of the entropy density jump Δs and, as a result, the position of the "equi-entropic" gauge, the thermodynamic relationships of the main text (Eqs. 1-5) are not affected: The Euler, Gibbs-Duhem, Clapeyron, and structural equations are still perfectly valid, and their nonequilibrium counterparts remain unchanged. Thus, without loss of generality, we simply ignore these quantum mechanical complications and use the expression given above for the ideal chemical potential. Thus, for each slab, we have $\mu_{\alpha,k}^{\text{id}} = -(3/2)T(z_k) \ln T(z_k) + T(z_k) \ln \bar{\rho}_{\alpha,k}$.

The excess chemical potential is calculated by the Widom insertion method (28). A particle of species α is inserted at a random position

in slab k , denoted \mathbf{r}_k , and the excess chemical potential follows from $\mu_{\alpha,k}^{\text{ex}} = -(k_B T/m) \ln \langle \exp[-(\Phi_k^{\alpha}(t)/k_B T)] \rangle$, where $\Phi_k^{\alpha} = \sum_j \phi_{\alpha \beta_j}(r_{jk})$ is the total interaction energy of the inserted particle, and the angled brackets represent an average over all possible insertion locations and all possible particle configurations. In a nonequilibrium scenario, the calculation is complicated by the fact that the temperature is not known a priori and can only be determined by analyzing the simulation data post hoc (see above). To circumvent this issue, at runtime, we record insertion energies in a histogram with a bin width of 0.0025ϵ . For insertions with interaction energies larger than 30ϵ , we simply keep a tally for normalization purposes, as the associated Boltzmann factors are essentially equal to zero to within machine precision. The minimum insertion energy captured in the histogram is -20ϵ , which is smaller than the interaction energy in a system of close-packed Lennard-Jones particles, ensuring that all insertions are properly recorded. We maintain a separate histogram for each slab, and, with proper normalization, obtain the probabilities $P_k(\Phi_l) \equiv P(\Phi_l^{\alpha} \approx \Phi_l)$, where $\Phi_l = -20\epsilon + (l - 1/2) \times 0.0025\epsilon$ is the energy associated with histogram bin l . The ensemble average is then performed in postprocessing once the kinetic temperature profile is known: $\mu_{\alpha,k}^{\text{ex}} = -(k_B T(z_k)/m) \ln \left\{ \sum_l P_k(\Phi_l) \exp[-\Phi_l/k_B T(z_k)] \right\}$. From our equilibrium simulations, we have found that, for the bin width chosen here, the error associated with the histogram procedure is orders of magnitude smaller than statistical error, and so use the same procedure in the nonequilibrium systems.

To ensure that the nonequilibrium simulations remain at steady-state conditions, we calculate the instantaneous energy flux $\mathbf{j}_{q,k}(t) = (1/V_s) \sum_i \mathbb{1}_{ki}(t) \left\{ \mathbf{v}_i(t) e_i(t) + (1/2) \sum_{j \neq i} \mathbf{r}_{ij} [\mathbf{f}_{ij} \cdot (\mathbf{v}_i + \mathbf{v}_j)] \right\}$, where $e_i(t)$ is the total energy of particle i at time t : $e_i = (1/2) [m\mathbf{v}_i^2(t) + \sum_{j \neq i} \phi_{\alpha_i \beta_j}(r_{ij})]$. We found that this energy flux as well as the species mass fluxes (equivalent to species momentum densities; see above) are constant to within statistical uncertainty throughout the production simulations and show no systematic deviations over time.

The NEMD code was written from scratch in C++ and was parallelized using the OpenMP library (48); it is freely available online (49). The simulations were conducted on 16 Intel Xeon E5 processors simultaneously on the Midway cluster of the Research Computing Center at the University of Chicago and took approximately 3 wk to complete. Analysis of the simulation data was performed using the Pandas (50), NumPy (51), SciPy (52), and CSAPS (53) Python packages. Figures were created with the Matplotlib package (54).

Data Availability. Selected data, including certain simulation output, analysis scripts, and processed data files used for figures have been archived in an open-access repository (55). Larger data files, such as simulation trajectories and particle insertion energy histograms, are available from the authors upon request. The simulation code is also freely available online (49).

ACKNOWLEDGMENTS. This work was supported by the University of Chicago Materials Research Science and Engineering Center, which is funded by the US NSF under Award DMR-2011854. P.M.R. is grateful to the NSF for the award of a Graduate Research Fellowship, Grant 1746045. Any opinions, findings, and conclusions or recommendations expressed in this material are those of the authors and do not necessarily reflect the views of the NSF. H.C.Ö. acknowledges the Pritzker School of Molecular Engineering and Eidgenössische Technische Hochschule (ETH) Zürich for support during his sabbatical stay at the University of Chicago.

Author affiliations: ^aPritzker School of Molecular Engineering, University of Chicago, Chicago, IL 60637; ^bDepartment of Materials, Eidgenössische Technische Hochschule (ETH) Zürich, CH-8093 Zürich, Switzerland; ^cMaterials Science Division, Argonne National Laboratory, Lemont, IL 60439; and ^dCenter for Molecular Engineering, Argonne National Laboratory, Lemont, IL 60439

1. J. S. Rowlinson, B. Widom, *Molecular Theory of Capillarity* (Clarendon Press Oxford, Oxford, United Kingdom, 1982).
2. J. Slattery, L. Sagis, E. S. Oh, *Interfacial Transport Phenomena* (Springer, New York), ed. 2, 2007.
3. L. M. Sagis, Dynamic properties of interfaces in soft matter: Experiments and theory. *Rev. Mod. Phys.* **83**, 1367-1403 (2011).

4. D. Venerus, H. Ottinger, *A Modern Course in Transport Phenomena* (Cambridge University Press, Cambridge, United Kingdom, 2018).
5. N. O. Jaensson, P. D. Anderson, J. Vermant, Computational interfacial rheology. *J. Non-Newtonian Fluid Mech.* **290**, 104507 (2021).

6. A. Lamorgese, R. Mauri, L. Sagis, Modeling soft interface dominated systems: A comparison of phase field and Gibbs dividing surface models. *Phys. Rep.* **675**, 1–54 (2017).
7. S. de Groot, P. Mazur, *Non-Equilibrium Thermodynamics* (North-Holland, Amsterdam, 1962).
8. H. Callen, *Thermodynamics and an Introduction to Thermostatistics* (Wiley, New York, ed. 2, 1985).
9. H. Struchtrup, *Macroscopic Transport Equations for Rarefied Gas Flows* (Springer, Berlin, 2005).
10. H. C. Öttinger, Thermodynamically admissible 13 moment equations from the Boltzmann equation. *Phys. Rev. Lett.* **104**, 120601 (2010).
11. S. Kjelstrup, D. Bedeaux, *Non-Equilibrium Thermodynamics of Heterogeneous Systems* (World Scientific, 2008).
12. V. K. Badam, V. Kumar, F. Durst, K. Danov, Experimental and theoretical investigations on interfacial temperature jumps during evaporation. *Exp. Therm. Fluid Sci.* **32**, 276–292 (2007).
13. E. Y. Gatapova *et al.*, The temperature jump at water–air interface during evaporation. *Int. J. Heat Mass Transf.* **104**, 800–812 (2017).
14. J. Niknejad, J. W. Rose, Interphase matter transfer: An experimental study of condensation of mercury. *Proc. R. Soc. Lond. A Math. Phys. Sci.* **378**, 305–327 (1981).
15. J. W. Gibbs, *The Scientific Papers of J. W. Gibbs: Thermodynamics* (Longmans, London, United Kingdom, 1906).
16. J. S. Rowlinson, Translation of J. D. van der Waals’ “The thermodynamik theory of capillarity under the hypothesis of a continuous variation of density.” *J. Stat. Phys.* **20**, 197–200 (1979).
17. J. W. Cahn, J. E. Hilliard, Free energy of a nonuniform system. I. Interfacial free energy. *J. Chem. Phys.* **28**, 258–267 (1958).
18. J. W. Cahn, Free energy of a nonuniform system. II. Thermodynamic basis. *J. Chem. Phys.* **30**, 1121–1124 (1959).
19. D. M. Anderson, G. B. McFadden, A. A. Wheeler, Diffuse-interface methods in fluid mechanics. *Annu. Rev. Fluid Mech.* **30**, 139–165 (1998).
20. J. G. Kirkwood, F. P. Buff, The statistical mechanical theory of surface tension. *J. Chem. Phys.* **17**, 338–343 (1949).
21. J. H. Irving, J. G. Kirkwood, The statistical mechanical theory of transport processes. IV. The equations of hydrodynamics. *J. Chem. Phys.* **18**, 817–829 (1950).
22. M. Grmela, H. C. Öttinger, Dynamics and thermodynamics of complex fluids. I. Development of a general formalism. *Phys. Rev. E Stat. Phys. Plasmas Fluids Relat. Interdiscip. Topics* **56**, 6620–6632 (1997).
23. H. C. Öttinger, M. Grmela, Dynamics and thermodynamics of complex fluids. II. Illustrations of a general formalism. *Phys. Rev. E Stat. Phys. Plasmas Fluids Relat. Interdiscip. Topics* **56**, 6633–6655 (1997).
24. H. Öttinger, *Beyond Equilibrium Thermodynamics* (Wiley, Hoboken, NJ, 2005).
25. T. Savin, K. S. Glavatskiy, S. Kjelstrup, H. C. Öttinger, D. Bedeaux, Local equilibrium of the Gibbs interface in two-phase systems. *Europhys. Lett.* **97**, 40002 (2012).
26. H. C. Öttinger, D. C. Venerus, Thermodynamic approach to interfacial transport phenomena: Single-component systems. *AIChE J.* **60**, 1424–1433 (2014).
27. D. Bedeaux, S. Kjelstrup, Fluid-fluid interfaces of multi-component mixtures in local equilibrium. *Entropy (Basel)* **20**, 250 (2018).
28. B. Widom, Some topics in the theory of fluids. *J. Chem. Phys.* **39**, 2808–2812 (1963).
29. M. Schweizer, H. C. Öttinger, T. Savin, Nonequilibrium thermodynamics of an interface. *Phys. Rev. E* **93**, 052803 (2016).
30. M. Kardar, *Statistical Physics of Fields* (Cambridge University Press, Cambridge, United Kingdom, 2007).
31. S. Cheng, J. B. Lechman, S. J. Plimpton, G. S. Grest, Evaporation of Lennard-Jones fluids. *J. Chem. Phys.* **134**, 224704 (2011).
32. F. Rahmani, T. Weathers, A. Hosangadi, Y. C. Chiew, A non-equilibrium molecular dynamics study of subcritical, supercritical and transcritical mixing of liquid-gas systems. *Chem. Eng. Sci.* **214**, 115424 (2020).
33. J. Ge, S. Kjelstrup, D. Bedeaux, J. M. Simon, B. Rousseau, Transfer coefficients for evaporation of a system with a Lennard-Jones long-range spline potential. *Phys. Rev. E Stat. Nonlin. Soft Matter Phys.* **75**, 061604 (2007).
34. M. L. Olivier, J. D. Rollier, S. Kjelstrup, Equilibrium properties and surface transfer coefficients from molecular dynamics simulations of two-component fluids. *Colloids Surf. A Physicochem. Eng. Asp.* **210**, 199–222 (2002).
35. I. Inzoli, S. Kjelstrup, D. Bedeaux, J. Simon, Thermodynamic properties of a liquid–vapor interface in a two-component system. *Chem. Eng. Sci.* **65**, 4105–4116 (2010).
36. I. Inzoli, S. Kjelstrup, D. Bedeaux, J. Simon, Transfer coefficients for the liquid–vapor interface of a two-component mixture. *Chem. Eng. Sci.* **66**, 4533–4548 (2011).
37. B. Hafskjold, T. Ikeshoji, S. Kjelstrup Ratkje, On the molecular mechanism of thermal diffusion in liquids. *Mol. Phys.* **80**, 1389–1412 (1993).
38. B. Hafskjold, S. K. Ratkje, Criteria for local equilibrium in a system with transport of heat and mass. *J. Stat. Phys.* **78**, 463–494 (1995).
39. J. J. Magda, M. Tirrell, H. T. Davis, Molecular dynamics of narrow, liquid-filled pores. *J. Chem. Phys.* **83**, 1888–1901 (1985).
40. T. Eckert, N. C. X. Stuhl Müller, F. S. Müller, M. Schmidt, Fluctuation profiles in inhomogeneous fluids. *Phys. Rev. Lett.* **125**, 268004 (2020).
41. C. Cercignani, M. Lampis, Kinetic models for gas–surface interactions. *Transp. Theory Stat. Phys.* **1**, 101–114 (1971).
42. G. S. Heffelfinger, F. Van Swol, Diffusion in Lennard-Jones fluids using dual control volume grand canonical molecular dynamics simulation (DCV-GCMD). *J. Chem. Phys.* **100**, 7548–7552 (1994).
43. G. Bussi, D. Donadio, M. Parrinello, Canonical sampling through velocity rescaling. *J. Chem. Phys.* **126**, 014101 (2007).
44. J. G. Briano, E. D. Glandt, Statistical thermodynamics of polydisperse fluids. *J. Chem. Phys.* **80**, 3336–3343 (1984).
45. D. A. Kofke, E. D. Glandt, Monte Carlo simulation of multicomponent equilibria in a semigrand canonical ensemble. *Mol. Phys.* **64**, 1105–1131 (1988).
46. D. Frenkel, B. Smit, *Understanding Molecular Simulation* (Academic, San Diego, CA, ed. 2, 2002).
47. H. C. Andersen, Molecular dynamics simulations at constant pressure and/or temperature. *J. Chem. Phys.* **72**, 2384–2393 (1980).
48. OpenMP Architecture Review Board, OpenMP application program interface version 5.0 (2018). <https://www.openmp.org/>. Accessed November 24, 2021.
49. P. M. Rauscher, Nonequilibrium simulations of interfaces (NESI). <https://github.com/depablogroup/NESI>. Deposited 2 November 2021.
50. W. McKinney, “Data structures for statistical computing in python” in *Proceedings of the 9th Python in Science Conference*, S. van der Walt, J. Millman, Eds. (SciPy, 2010), pp. 56–61.
51. C. R. Harris *et al.*, Array programming with NumPy. *Nature* **585**, 357–362 (2020).
52. P. Virtanen *et al.*, SciPy 1.0 Contributors, SciPy 1.0: Fundamental algorithms for scientific computing in Python. *Nat. Methods* **17**, 261–272 (2020).
53. E. Prilepin, CSAPS – Cubic Spline Approximation (Smoothing) version 1.1.0. (2021). <https://csaps.readthedocs.io/>. Accessed 24 November 2021.
54. J. D. Hunter, Matplotlib: A 2D graphics environment. *Comput. Sci. Eng.* **9**, 90–95 (2007).
55. P. M. Rauscher, H. C. Öttinger, J. J. de Pablo, *Data archive for “Nonequilibrium statistical thermodynamics of multicomponent interfaces.”* Zenodo. <https://zenodo.org/record/5725182#.Yk7bMS-B3vw>. Deposited 24 November 2021.